J Physiol 594.21 (2016) pp 6395–6405

The Journal of Physiology

Eliminating Nox2 reactive oxygen species production protects dystrophic skeletal muscle from pathological calcium influx assessed *in vivo* by manganese-enhanced magnetic resonance imaging

James A. Loehr[1], Gary R. Stinnett[1], Mayra Hernández-Rivera[2], Wesley T. Roten[3,4], Lon J. Wilson[2], Robia G. Pautler[1] and George G. Rodney[1]

[1] *Department of Molecular Physiology and Biophysics, Baylor College of Medicine, Houston, TX, USA*
[2] *Department of Chemistry, Rice University, Houston, TX, USA*
[3] *SMART Program, Baylor College of Medicine, Houston, TX, USA*
[4] *Department of Biology, University of North Carolina, Chapel Hill, NC, USA*

Key points

- Inhibiting Nox2 reactive oxygen species (ROS) production reduced *in vivo* calcium influx in dystrophic muscle.
- The lack of Nox2 ROS production protected against decreased *in vivo* muscle function in dystrophic mice.
- Manganese-enhanced magnetic resonance imaging (MEMRI) was able to detect alterations in basal calcium levels in skeletal muscle and differentiate disease status.
- Administration of Mn^{2+} did not affect muscle function or the health of the animal, and Mn^{2+} was cleared from skeletal muscle rapidly.
- We conclude that MEMRI may be a viable, non-invasive technique to monitor molecular alterations in disease progression and evaluate the effectiveness of potential therapies for Duchenne muscular dystrophy.

Abstract Duchenne muscular dystrophy (DMD) is an X-linked progressive degenerative disease resulting from a mutation in the gene that encodes dystrophin, leading to decreased muscle mechanical stability and force production. Increased Nox2 reactive oxygen species (ROS) production and sarcolemmal Ca^{2+} influx are early indicators of disease pathology, and eliminating Nox2 ROS production reduces aberrant Ca^{2+} influx in young *mdx* mice, a model of DMD. Various imaging modalities have been used to study dystrophic muscle *in vivo*; however, they are based upon alterations in muscle morphology or inflammation. Manganese has been used for indirect monitoring of calcium influx across the sarcolemma and may allow detection of molecular alterations in disease progression *in vivo* using manganese-enhanced magnetic resonance imaging (MEMRI). Therefore, we hypothesized that eliminating Nox2 ROS production would decrease calcium influx in adult *mdx* mice and that MEMRI would be able to monitor and differentiate disease status in dystrophic muscle. Both *in vitro* and *in vivo* data demonstrate that eliminating Nox2 ROS protected against aberrant Ca^{2+} influx and improved muscle function in dystrophic muscle. MEMRI was able to differentiate between different pathological states *in vivo*, with no long-term effects on animal health or muscle function. We conclude that MEMRI is a viable, non-invasive technique to differentiate disease status and might provide a means to monitor and evaluate the effectiveness of potential therapies in dystrophic muscle.

(Received 16 June 2016; accepted after revision 12 August 2016; first published online 24 August 2016)
Corresponding author G. G. Rodney: Baylor College of Medicine, Department of Molecular Physiology and Biophysics, One Baylor Plaza-BCM335, Houston, TX 77030, USA. Email: rodney@bcm.edu

DOI: 10.1113/JP272907

Abbreviations BW, body weight; Ca^{2+}, calcium; CT, computed tomography; DMD, Duchene muscular dystrophy; EDL, extensor digitorum longus; ICP-MS, inductively coupled plasma–mass spectrometry; Mn^{2+}, manganese; $MnCl_2$, manganese chloride; MEMRI, manganese-enhanced magnetic resonance imaging; MnR, manganese Ringer; MRI, magnetic resonance imaging; *mdx* mouse, Duchenne muscular dystrophy mouse; Nox2, NADPH oxidase 2; NR, normal Ringer; SNR, signal-to-noise ratio; ROS, reactive oxygen species; ROI, region of interest; T1, longitudinal relaxation time constant; T2, transverse relaxation time; WT, wild-type.

Introduction

Duchene muscular dystrophy (DMD) is an X-linked recessive disease, which affects one in every 3500 boys, resulting in progressive muscle atrophy, loss of ambulation and death from cardiac or respiratory failure (Levi *et al.* 2015). A variety of standard outcome measures, such as muscle strength, timed motor performance and pulmonary function tests, have been used to assess the functional ability and disease progression in DMD patients (Bushby & Connor, 2011). However, many of these tests are affected by the level of effort and mood of the patient, and most of the studies have evaluated ambulatory patients over the age of 6 years, leaving in question their application to patients of different ages with different levels of functional ability (Bushby & Connor, 2011; Rutkove *et al.* 2014).

Various imaging modalities, such as computed tomography (CT), magnetic resonance imaging (MRI) and ultrasound, have been used with the intent of removing patient subjectivity during testing in order to quantify and monitor disease progression non-invasively over the entire range of ages and functional abilities (Rutkove *et al.* 2014; Willcocks *et al.* 2014, 2016; Shklyar *et al.* 2015; Zaidman *et al.* 2015; Hogrel *et al.* 2016). Computed tomography and ultrasound possess several limitations that hinder their use owing to concerns with radiation, depth of imaging and inter- and intra-operator reliability (Ortolan *et al.* 2015). Magnetic resonance imaging (MRI) is a useful tool for imaging dystrophic muscle; however, early in disease progression the MRI scans may appear normal given that the technique relies upon the appearance of morphological alterations such as increased inflammation, fibrosis or fatty infiltrates (Ortolan *et al.* 2015). In addition, the morphological alterations can be influenced by ethnicity and adaptations due to exercise (Ortolan *et al.* 2015). Therefore, the ability to image molecular alterations in disease pathology, such as calcium influx, may provide a more sensitive measure for tracking disease progression throughout the life of the patient.

Muscular dystrophy is characterized by increased membrane permeability to calcium (Ca^{2+}), resulting in greater Ca^{2+} influx across the sarcolemma (Tutdibi *et al.* 1999; De Backer *et al.* 2002; Pal *et al.* 2014), and increased NADPH oxidase 2 (Nox2)-derived reactive oxygen species (ROS; Whitehead *et al.* 2010; Pal *et al.* 2014). Previous studies have shown that Ca^{2+} channel activity (Franco-Obregon & Lansman, 1994; Vasquez *et al.* 2012) and Nox2 content and activity (Whitehead *et al.* 2010) are upregulated before the onset of other pathological symptoms (i.e. immune cell infiltration, oedema and fibrosis). Blocking Ca^{2+} channels or down-regulating Nox2 ROS production in young (5-week-old) *mdx* mouse muscle reduces aberrant sarcolemmal Ca^{2+} influx and alleviates the pathophysiology associated with dystrophic muscle (Altamirano *et al.* 2013; Pal *et al.* 2014). These data support the idea that aberrant ROS production and sarcolemmal Ca^{2+} influx are crucial early events in the pathophysiology of DMD, prior to the onset of observable histological muscle damage and inflammation.

One *in vitro* method to assess Ca^{2+} influx across the sarcolemma is to monitor manganese (Mn^{2+}) quench of the fluorescence of fura-2 (Tutdibi *et al.* 1999; Pal *et al.* 2014), which is a sensitive indicator dye for measuring intracellular Ca^{2+}. Mn^{2+} is a divalent cation similar in ionic radius and chemical properties to Ca^{2+} that can pass through various Ca^{2+} channels, and its paramagnetic properties make it a potent MRI spin lattice relaxation time constant (T1) contrast agent (Naruse & Sokabe, 1993; Dryselius *et al.* 1999; Takeda, 2003; Waghorn *et al.* 2009). Manganese-enhanced MRI (MEMRI) has been used to assess various conditions associated with Ca^{2+} ions, such as brain activity (Cha *et al.* 2016; Schroeder *et al.* 2016), neuronal tract tracing and axonal transport (Inoue *et al.* 2011; Majid *et al.* 2014), injury (Rodriguez *et al.* 2016; Yang *et al.* 2016), ischaemia–reperfusion (Zhao *et al.* 2015) and cardiac function (Chen *et al.* 2012; Andrews *et al.* 2015). However, it has never been used to assess aberrant Ca^{2+} handling in dystrophic skeletal muscle. Therefore, we hypothesized that eliminating Nox2 ROS production would decrease aberrant Ca^{2+} influx and that MEMRI would be able to differentiate disease status in dystrophic muscle.

Methods

Ethical approval

All animal procedures were performed in accordance with National Institutes of Health guidelines and approved by the Institutional Animal Care and Use Committee of Baylor College of Medicine.

Animals

C57Bl/6J [wild-type (WT)] and C57Bl/10ScSn-Dmdmdx/J (*mdx*) mice were purchased from Jackson Laboratories (Bar Harbor, ME, USA) and bred following their breeding strategy. To generate *mdx* animals lacking Nox2 ROS production, mice lacking $p47^{phox}$ [B6(Cg)-Ncf1m1J/J, JaxMice], a Nox2 subunit, were crossed with dystrophin-deficient mice (C57BL/10ScSn-Dmdmdx/J) to generate $p47^{phox\,(-/-)}$/dystrophin-deficient $^{(-/y)}$ mice ($p47^{-/-}$/*mdx*; Pal *et al.* 2014). All mice had *ad libitum* access to food and water. At ∼5 months of age, mice were anaesthetized by isoflurane (2%) inhalation for either *in vivo* experiments or killed by rapid cervical dislocation for *in vitro* assays.

In vitro force measurements

The extensor digitorum longus (EDL) muscle was surgically dissected. One end of the EDL was attached to a fixed hook and the other to a force transducer (F30; Harvard Apparatus, Holliston, MA, USA) using silk suture (4–0). The muscle was placed in a physiological saline solution containing (mM): 2.0 $CaCl_2$, 120.0 NaCl, 4.0 KCl, 1.0 $MgSO_4$, 25.0 $NaHCO_3$, 1.0 KH_2PO_4 and 10.0 glucose, pH 7.3, and continuously gassed with 95% O_2–5% CO_2 at 25°C. Each EDL was incubated at 30°C for 15 min, after which optimal muscle length (L_o) and voltage (V_{max}) were adjusted to elicit the maximal twitch force. The 95% O_2–5% CO_2 solution was changed to either a $CaCl_2$ (NR) or a $MnCl_2$-modified Ringer (MnR) solution, which was at 30°C, containing (mM): 1.8 $CaCl_2$ or $MnCl_2$, 120.0 NaCl, 4.7 KCl, 0.6 $MgSO_4$, 1.6 $NaHCO_3$, 0.13 NaH_2PO_4, 7.8 glucose and 20.0 Hepes, pH 7.3. Each EDL was incubated in its respective solution for 2 min, followed by establishing a force–frequency relationship. Force–frequency characteristics were measured at stimulation frequencies of 1, 10, 20, 40, 80, 120 and 150 Hz every minute with pulse and train durations of 0.5 and 250 ms, respectively. At the end of the contractile protocol, muscle length was measured using hand-held electronic callipers, and fibre bundles were trimmed of excess connective tissue, blotted dry and weighed. Muscle weight and L_o were used to estimate cross-sectional area, and absolute forces were expressed in newtons per centimetre squared (Close, 1972).

Manganese quench assay

Flexor digitorum brevis muscle was surgically isolated and incubated in minimal essential media containing 1% penicillin (10,000 U/ml) and streptomycin (10,000 micrograms/ml) (Pen Strep; Life Technologies, Grand Island, NY, USA) and 0.4% collagenase A (Roche Applied Science, Indianapolis, IN, USA) at 37°C for 2.0 h. To release single fibres, flexor digitorum brevis muscles were gently triturated in minimal essential media containing 10% fetal bovine serum and 1% Pen Strep and incubated in 5% CO_2 at 37°C until used, typically 12–36 h later. The fibres were then plated on gel from Engelbreth–Holm–Swarm (ECM) murine sarcoma (Sigma-Aldrich, St Louis, MO, USA)-coated 96-well culture plates (Greiner Bio-one, Monroe, NC, USA), washed with a Ca^{2+}-based Hepes modified Ringer solution and incubated with fura-2 AM (5 μM; TEFLabs, Austin, TX, USA) for 30 min at room temperature. Prior to microscopy, fibres were washed again with a Ca^{2+}-based Hepes modified Ringer solution, and the dye was allowed to de-esterify for 20 min at room temperature. Fura-2 excitation (360 nm/380 nm) and emission (510 nm) were monitored using the IonOptix Myocyte Calcium and Contractility Recording System (IonOptix, Westwood, MA, USA). Baseline fluorescence measurements were monitored for 1 min in a Ca^{2+}-based Hepes modified Ringer solution; the buffer was then replaced with a Mn^{2+}-based Hepes modified Ringer solution and monitored for an additional 3.5 min. Data were imported into OriginPro 2015 (OriginLab, Northampton, MA, USA) and, using the 360 nm signal, the background fluorescence rate was subtracted from the Mn^{2+} quench rate for each cell and normalized to the average rate calculated for WT cells.

Manganese-enhanced MRI

Animal body weight (BW) was measured 2 days before, on the day of administration and 2 days after either Mn^{2+}–bicine or bicine-only control buffer. Mice were anaesthetized by inhalation of isoflurane (2%) and given a 40 mg kg^{-1} I.V. tail infusion (0.4 ml h^{-1}) of manganese (II) chloride tetrahydrate ($MnCl_2$; Sigma-Aldrich, St Louis, MO, USA) dissolved in a bicine (Sigma-Aldrich) buffer or a bicine-only solution (50 mM). The hindlimb lower legs of each mouse were imaged 30 min and 2 days postinfusion. Mice were placed in the prone position on a custom-built holder, and using a bite bar, the head was secured into a head/nose cone. The hindlimbs were extended, with the feet plantar flexed and individually secured to the holder using tape. The position of the mouse allowed for a head-first entry as the custom-built holder entered the magnet. While in the magnet, an air heating system (SA Instruments Inc., Stony Brook, NY, USA) was used to maintain body temperature at 37°C, and a rectal probe and a pressure pad, placed beneath the animal, were used to monitor temperature and respiratory rate, respectively, using the Model 1025 Small Animal Monitoring & Gating System software (SA Instruments Inc.).

Magnetic resonance images were acquired on a 9.4 T Bruker AvanceBiospec Spectrometer, 21-cm-bore horizontal scanner with a 35 mm volume resonator (Bruker BioSpin, Billerica, MA, USA) with Paravision 5.1

software (Bruker Biospin). Once positioned in the magnet, a FLASH tripilot multisequence scan was performed to ensure that the legs were ideally positioned for the volume coil. Legs were imaged using a T1-weighted 2D RARE sequence with fat suppression. Imaging parameters for MEMRI scans were as follows: repetition time (TR) = 614.3 ms, echo time (TE) = 7.6 ms, radio frequency (RF) = 2, field of view (FOV) = 4 cm × 3 cm, slice thickness = 1 mm with no interslice gap, matrix size = 256 × 256, 15 slice, 3 m, 55 s and 910 ms. The default Paravision software fat suppression method was employed using the a −3.5 ppm offset with a gauss512 pulse shape, a 1040.1 Hz bandwidth, a spoiler duration of 2 ms and a spoiler strength of 20%.

Magnetic resonance image processing

To measure the volume of muscle with enhanced Mn^{2+} contrast, images were imported into Amira 5.1, and regions of interest (ROI) for the soft tissue were masked for the right and left legs. A background four corners mask was also made for the signal-to-noise ratio (SNR) calculation. Scans were reconstructed with absolute mapping to raw 2dseq files, and the 2dseq files and mask files were imported into Matlab (Mathworks, Natick, MA, USA) for processing. Analysis for enhancement consisted of application of an SNR cut-off and distribution analysis of that ROI on each slice. The SNR was calculated using the four corners background and ROI mask method using $SNR = R \times S_{ROI}/SD_{AIR}$ where R is the Rician distribution factor, S_{ROI} is the mean signal in the ROI being analysed and SD_{AIR} is the standard deviation of the air signal found using the background four corners mask (Dietrich *et al.* 2007). If the SNR was below $R \times 25$, that ROI slice was not used for analysis. Evaluation of post-SNR processed data revealed a >94% inclusion of voxels for analysis. Semi-automatic selection of muscle enhancement was applied by using a threshold of two standard deviations above the ROI median signal intensity (Durmus *et al.* 2012; Vohra *et al.* 2016). Each ROI was processed individually for SNR and threshold, and enhanced voxels were calculated as the number of voxels above the previously described threshold divided by ROI size, without slices discounted by SNR. Owing to the focal, inhomogeneous and differential involvement of pathology within the same muscle in *mdx* mice, the lower leg muscle enhancement was calculated as the number of enhanced voxels divided by the total processed volume.

In vivo force measurements

Dorsiflexor (tibialis anterior and extensor digitorum longus) force was measured using a dual-mode lever system (305C-LR-FP) with electrical stimulation (701C; Aurora Scientific Inc., Aurora, ON, Canada) 2 days prior to, immediately after and 2 days after buffer administration. On the day of buffer infusion, force was measured within 2 h of buffer administration and immediately after MRI. While anaesthetized, mice were placed on their back, the knee joint was immobilized, and the foot was secured into a footplate. Needle electrodes were inserted below the knee joint, just underneath the skin but above the tibialis anterior. A 1 Hz stimulus was administered to determine optimal electrode placement, and after 1 min the force was measured using a 150 Hz stimulus. Data were analysed using the dynamic muscle control and analysis software (Aurora Scientific Inc.).

Elemental analysis of Mn^{2+}

Inductively coupled plasma–mass spectrometry (ICP-MS) was used to obtain the Mn^{2+} concentration quantitatively in different tissues. Using the same $MnCl_2$ administration protocol as MEMRI, Mn^{2+} levels in the muscles of the lower leg (gastrocnemius, soleus, tibialis anterior and EDL) and the kidneys were measured in non-infused and $MnCl_2$-infused mice after 30 min and 2 days. After the mice were killed, all tissues were frozen in liquid nitrogen and stored at −80°C. Tissue samples were lyophilized for 48 h and subsequently placed in glass scintillation vials. Seventy per cent HNO_3, trace-metal grade (Sigma-Aldrich) was regularly added to the samples while under heat to digest the organic matter. After 7–10 days of constant acid exposure, samples appear as a clear or light yellow liquid. Samples were diluted to 5 ml with an aqueous solution of 2% HNO_3, trace-metal grade and 2% ethanol HPLC grade (CHROMASOLV®; Sigma-Aldrich), and filtered using a syringe filter (0.22 μm pore size). All samples were analysed with a NexION 300 ICP-MS (PerkinElmer, Waltham, MA, USA), using lutetium as the internal standard.

Data analysis

A one-way ANOVA was used to measure statistical differences between groups for the Mn^{2+} quench assay and frequency specific force production. Two-way and two-way repeated-measures ANOVAs were used where appropriate to determine statistical differences between groups for all other data. Tukey's *post hoc* test was used when statistical differences were identified. A linear regression analysis was performed to assess the correlation between enhanced voxels assessed by MEMRI and *in vivo* muscle function. Statistical analysis was performed in Origin Pro (OriginLab Corporation, Northhampton, MA, USA), with significance set *a priori* at $P \leq 0.05$. Data are reported as the means ± SEM, unless otherwise specified.

Results

Genetic deletion of Nox2 activity attenuates Mn^{2+} influx and recovers force deficits in adult *mdx* skeletal muscle

Sarcolemmal Ca^{2+} influx is measured indirectly by Mn^{2+} entry into the cell and quantified using the rate of dye quench (Tutdibi *et al.* 1999; De Backer *et al.* 2002; Pal *et al.* 2014). Skeletal muscles of *mdx* mice are known to have elevated Mn^{2+}/Ca^{2+} influx (Pal *et al.* 2014) and decreased force production (Pal *et al.* 2014). Alterations in ROS production have been shown to affect both Ca^{2+} handling and force production (Pal *et al.* 2014). Here, we demonstrated that adult *mdx* mice had an increase in sarcolemmal Mn^{2+} influx and that eliminating Nox2 ROS production reduced that influx back to WT levels ($P \leq 0.05$; Fig. 1*A*). The lack of Nox2 ROS production improved EDL muscle function at or above 80 Hz compared with *mdx* animals (Fig. 1*B*). In addition, Mn^{2+} had no effect on EDL muscle function for any of the genotypes at any tested frequency (Fig. 1*B*). Taken together, these data indicate that reducing Nox2 ROS production improves *mdx* pathology (decreased sarcolemmal Ca^{2+} influx and increased muscle force production) and provide evidence that Mn^{2+} administration should not alter muscle function following MEMRI.

Eliminating Nox2 ROS production decreases aberrant sarcolemmal Ca^{2+} permeability in dystrophic muscle: differentiation of disease status by MEMRI

Mn^{2+} can enter skeletal muscle fibres, as indicated by our Mn^{2+} quench data, is paramagnetic, and has been used as an MRI contrast agent (Naruse & Sokabe, 1993; Dryselius *et al.* 1999; Takeda, 2003; Waghorn *et al.* 2009; Inoue *et al.* 2011; Majid *et al.* 2014). In this study, we used MEMRI to determine the volume of muscle with enhanced Mn^{2+} contrast. Representative MEMRI images illustrate enhanced contrast in the lower leg of both *mdx* and $p47^{-/-}/mdx$ mice compared with WT mice or bicine controls (Fig. 2*A*). Quantification revealed *in vivo* enhanced contrast in the lower limb of *mdx* mice compared with both WT and $p47^{-/-}/mdx$ animals 30 min postinfusion ($P \leq 0.05$; Fig. 2*B*). Although the $p47^{-/-}/mdx$ animals showed greater enhanced contrast compared with WT mice, the contrast level was lower than that observed with the *mdx* animals ($P \leq 0.05$; Fig. 2*B*). Two days after $MnCl_2$ injection, both *mdx* and $p47^{-/-}/mdx$ contrast was reduced to WT levels and the values were not different from bicine-injected control mice, indicating that animals had returned to baseline levels (Fig. 2*B*).

Inductively coupled plasma–mass spectrometry confirmed an increase in lower leg muscle Mn^{2+} content 30 min postinjection. Muscle Mn^{2+} content in *mdx* mice was elevated above WT levels ($P \leq 0.05$) and showed a trend to be elevated above $p47^{-/-}/mdx$ mice ($P = 0.07$), in agreement with the MEMRI data (Fig. 3). The Mn^{2+} levels were reduced to near baseline levels 2 days postinjection (Fig. 3).

The kidney participates in overall Mn^{2+} clearance from the body (Kato, 1963; Gerdin, 1985; Hu *et al.* 2011); therefore, using ICP-MS we evaluated the Mn^{2+}

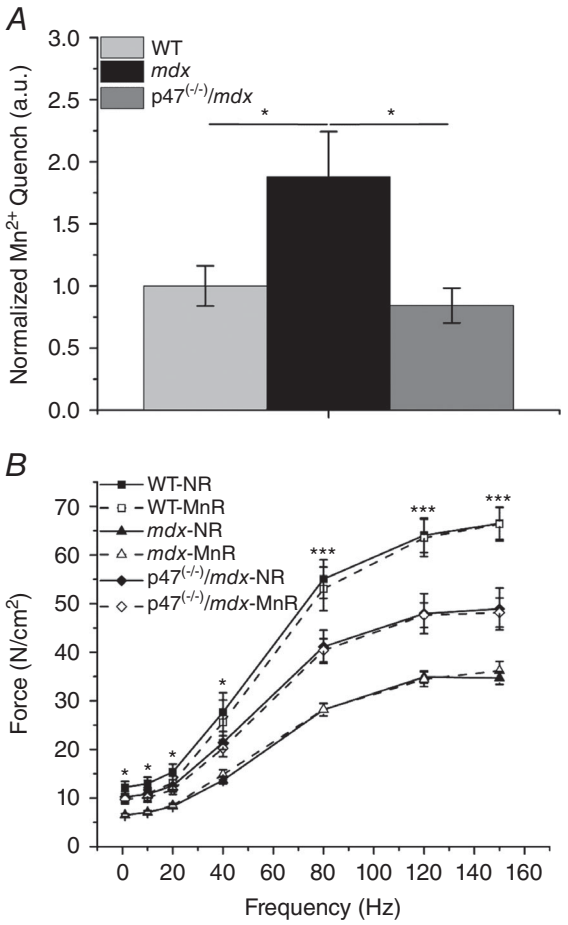

Figure 1. Eliminating Nox2 reactive oxygen species (ROS) production reduces Mn^{2+} influx and protects against force decrements in *mdx* muscle
A, sarcolemmal Mn^{2+} influx is elevated in flexor digitorum brevis fibres of adult *mdx* skeletal muscle compared with both wild-type (WT) and $p47^{-/-}/mdx$ muscle, $^{*}P \leq 0.05$. *B*, All three genotypes were significantly different from one another at stimulation frequencies ≥80 Hz, $^{***}P \leq 0.05$. Extensor digitorum longus (EDL) force from WT mice only was greater than that of *mdx* mice at stimulation frequencies <40 Hz, $^{*}P \leq 0.05$. There were no significant differences in force production between EDL muscle in normal Ringer solution (NR; filled symbols and continuous lines) and manganese Ringer solution (MnR; open symbols and dashed lines). Data (means ± SEM) are representative of at least five fibres from at least three animals for Mn^{2+} quench and at least five animals for force frequency.

concentration in the kidney as an indicator of Mn^{2+} clearance. Inductively coupled plasma–mass spectrometry data demonstrated elevated Mn^{2+} content in the kidney 30 min postinjection that was reduced to baseline levels by 2 days (Fig. 3), indicating that the kidney is not accumulating Mn^{2+} and is likely clearing it from the system.

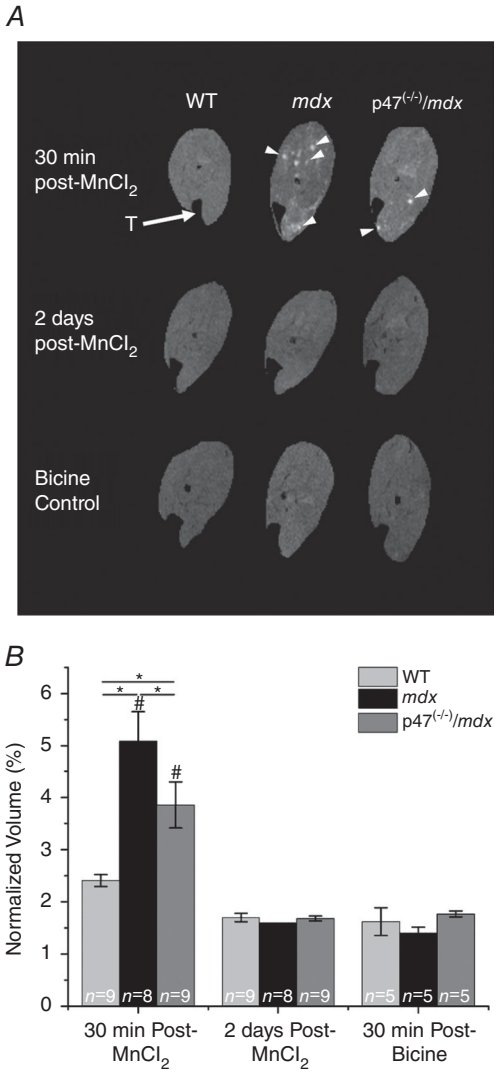

Figure 2. Nox2 ROS promote sarcolemmal Ca^{2+} permeability
A, representative magnetic resonance images. Both *mdx* and p47$^{-/-}$/*mdx* mice displayed enhanced contrast (arrowheads) 30 min after $MnCl_2$ administration compared with WT mice. Enhanced contrast was almost completely dissipated 2 days postadministration in all three genotypes and was similar to the bicine control buffer images at 30 min after bicine administration. T (arrow) indicates the tibia. *B*, at 30 min postinfusion, the lower leg of *mdx* mice showed enhanced contrast compared with WT mice, while the p47$^{-/-}$/*mdx* mice demonstrated reduced enhanced voxels compared with *mdx* mice, $^{*}P \leq 0.05$. Enhanced contrast was significantly different between 30 min post- and 2 days post-$MnCl_2$ administration for both *mdx* and p47$^{-/-}$/*mdx* mice, $^{\#}P \leq 0.05$. All mice returned to baseline values 2 days later, given that there were no differences between the 2 days post-$MnCl_2$ and 30 min post-bicine control buffer. Data are means ± SEM unless otherwise noted.

Nox2 ROS promotes *in vivo* torque loss in dystrophic muscle

Change in BW is used to assess animal health/disease severity, with a 10–15% decrease in BW within a few days taken to be crucial to the animal's health and a criterion for euthanasia (Foltz & Ullman-Cullere, 1999; Ray *et al.* 2010). Although there were initial differences in BW between the various genotypes (Fig. 4*A*), the administration of either $MnCl_2$ or bicine had no effect on BW over the course of the protocol (Fig. 4*B*). These data indicate that $MnCl_2$ injection had no negative effects on animal health over the course of the study.

We have shown protections against decreased *in vitro* force production in both diaphragm (Pal *et al.* 2014) and EDL (Fig. 1*B*) upon eliminating Nox2 ROS in *mdx* mice. Here, we demonstrated a 42% loss of *in vivo* dystrophic muscle function compared with a 20% decrement in the p47$^{-/-}$/*mdx* mice, a 53% protection against dystrophy-induced torque loss (Fig. 4*C*). Administration of $MnCl_2$ had no effect on *in vivo* muscle function compared with the bicine controls (Fig. 4*D*). Torque production in WT and p47$^{-/-}$/*mdx* mice did not change over the course of the study; however, *mdx* animals demonstrated an increase in torque following $MnCl_2$ administration that was maintained 2 days postinjection

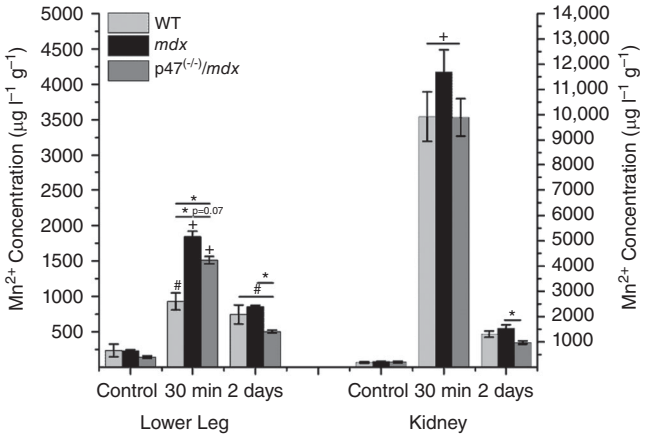

Figure 3. Reduced muscle Mn^{2+} concentration upon inhibition of Nox2 ROS
The concentration of Mn^{2+} increased 30 min postinfusion in both the lower leg and the kidney. The *mdx* mice showed greater Mn^{2+} accumulation than WT, whereas p47$^{-/-}$/*mdx* demonstrated a trend to have less Mn^{2+} accumulation than *mdx* mice in the lower leg; $P \leq 0.05$ $^{\#}$ *vs.* control, $^{+}$ *vs.* control and 2 days, and * between groups. Data (means ± SEM) are representative of at least three animals.

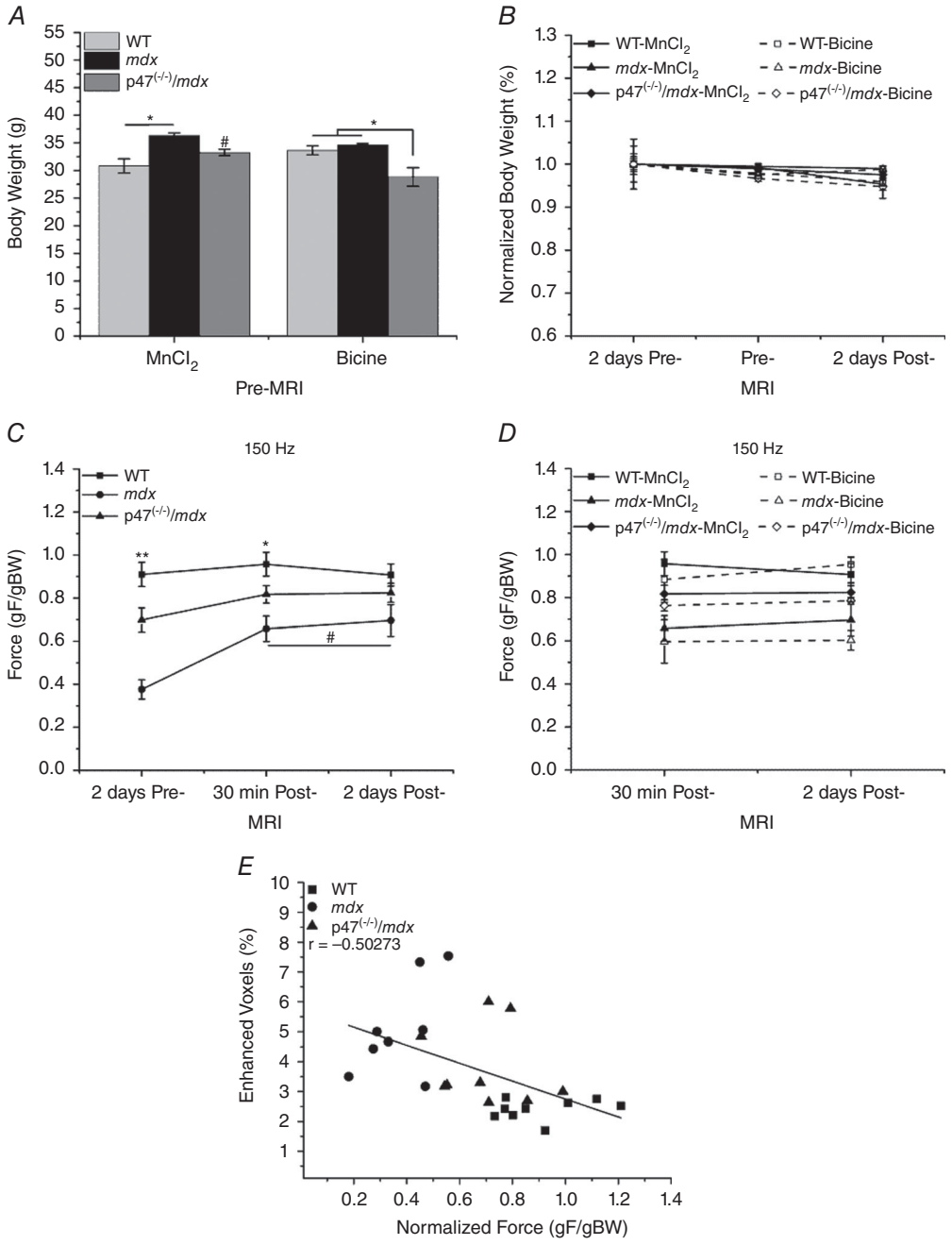

Figure 4. Inhibition of Nox2 ROS protects against *in vivo* torque loss in dystrophic muscle
A, initial body weight (BW) was different between WT and *mdx* mice within the $MnCl_2$ group and between p47$^{-/-}$/*mdx* and both WT and *mdx* mice in the bicine control group, $^{*}P \leq 0.05$. Initial BW was different between p47$^{-/-}$/*mdx* $MnCl_2$ and p47$^{-/-}$/*mdx* bicine-only groups, $^{\#}P \leq 0.05$. *B*, within each genotype, administration of either $MnCl_2$ (filled symbols and continuous lines) or the bicine control buffer (open symbols and dashed lines) had no effect on BW over the course of the study. *C*, prior to buffer administration, WT, *mdx* and p47$^{-/-}$/*mdx* muscle force production were statistically different from one another, $^{**}P \leq 0.05$. After $MnCl_2$ administration at the 30 min post-MRI, only WT was different from *mdx*, $^{*}P \leq 0.05$. There were no significant differences in force production between groups after $MnCl_2$ administration at the 2 days post-MRI. Force production increased in *mdx* mice after $MnCl_2$ injection at the 30 min post- and 2 days post-MRI compared with pre-MRI force production, $^{\#}P \leq 0.05$. *D*, there were no significant differences in force production within any genotype after $MnCl_2$ (filled symbols and continuous lines) or bicine administration (open symbols and dashed lines) at the 30 min post- or 2 days post-MRI. *E*, there was a significant correlation between enhanced contrast and normalized force ($P \leq 0.05$). Force was normalized to BW (gF/gBW) because of the initial BW differences observed in *C*. Data are from at least five animals and are represented as means ± SEM.

(Fig. 4*C*). In addition, we demonstrated a significant correlation ($r = -0.50273$) between enhanced contrast and muscle function (Fig. 4*E*). Taken together, we demonstrated that eliminating Nox2 ROS production protected against *in vivo* torque loss in *mdx* skeletal muscle, $MnCl_2$ had no negative effects on muscle function, and decreased muscle function was associated with enhanced sarcolemmal Mn^{2+} permeability.

Discussion

Dystrophic muscle is characterized by elevated Mn^{2+}/Ca^{2+} influx across the sarcolemma. Previously, we have shown in young *mdx* mice that eliminating Nox2 ROS production reduced this influx to WT levels (Pal *et al.* 2014). Here, we confirmed the increased *in vitro* Mn^{2+}/Ca^{2+} influx in adult *mdx* muscle and extended these findings to include increased *in vivo* Mn^{2+}/Ca^{2+} accumulation using a novel technique in skeletal muscle, MEMRI. In addition, eliminating Nox2 ROS in dystrophic muscle protected against that aberrant Ca^{2+} influx both *in vitro* and *in vivo* and recovered significant muscle function compared with dystrophic muscle. Using MEMRI, we were able to monitor changes in contrast intensity over time and differentiate between dystrophic muscle and a treatment group which partly protected against the functional deficits observed in dystrophic muscle. Although it has been possible to detect differences in dystrophic pathology with other imaging modalities (Fan *et al.* 2014; Rutkove *et al.* 2014; Willcocks *et al.* 2014, 2016; Shklyar *et al.* 2015; Zaidman *et al.* 2015; Hogrel *et al.* 2016), they are dependent upon alterations in muscle volume, the development of fibrosis or an increase in fatty infiltrates to detect changes in muscle quality. Although it has been possible to detect molecular alterations in dystrophic muscle with positron emission tomography (Ahmad *et al.* 2011), to the best of our knowledge the present study is the first investigation to demonstrate the ability of an MRI modality to use molecular alterations in dystrophic muscle to detect differences between dystrophic and healthy muscle as well as to differentiate between dystrophic muscle and a treatment group genetically modified to reduce the pathology.

Although we were able to detect differences in the disease status of dystrophic muscle with MEMRI, it was important to determine whether $MnCl_2$ accumulated or adversely affected muscle function, given that muscle function in dystrophic patients is progressively compromised (Beenakker *et al.* 2005). Previously, Dodd *et al.* (2005) have shown that acute $MnCl_2$ administration had no effect on grip strength or endurance, in agreement with our *in vitro* and *in vivo* muscle function data. In addition, we found a slight increase in *in vivo* force production in *mdx* mice following $MnCl_2$ administration that was sustained 2 days postinjection. Dystrophic skeletal muscle is characterized by increased ROS production (Whitehead *et al.* 2008, 2010; Pal *et al.* 2014; Kozakowska *et al.* 2015), and Mn^{2+} has been shown to possess an antioxidant capacity (Coassin *et al.* 1992; Barandier *et al.* 1998; Eybl & Kotyzová, 2010). In addition, Mn^{2+} has been used as the backbone in several synthetic antioxidants that demonstrated beneficial effects on muscle function (Doctrow *et al.* 2002; Kim & Lawler, 2012; Yamada *et al.* 2015). We are currently investigating whether the improved muscle function observed in *mdx* mice with Mn^{2+} administration is attributable to alterations in redox balance.

Although Mn^{2+} administration had no negative effect on muscle function, there was concern that Mn^{2+} might accumulate within cells and result in toxicity. The clearance of Mn^{2+} from most organ systems, except for the brain, appears to occur quickly (1–3 days) following an acute I.V. injection of $MnCl_2$ (Kato, 1963; Ni *et al.* 1997; Takeda *et al.* 1998). Our MEMRI and ICP-MS data are in agreement, because both skeletal muscle and the kidneys demonstrated a rapid clearance of Mn^{2+} by 2 days post-injection. In the brain, acute dosing results in a biphasic increase in brain Mn^{2+} levels (Sotogaku *et al.* 2000) that peaks around 24 h (Gallez *et al.* 1997; Ni *et al.* 1997; Sotogaku *et al.* 2000), followed by a slow gradual decline in Mn^{2+} levels (Gallez *et al.* 1997; Takeda *et al.* 1998). Using similar $MnCl_2$ concentrations, Dodd *et al.* (2005) found minimal to no neurological deficits after tail vein injection. However, Ponzoni *et al.* (2002) found significant functional motor impairment after direct injection into the brain. Differences in the results may be explained by the different methods of administration, with tail vein injection (Dodd *et al.* 2005) resulting in a lower concentration delivered to the brain *vs.* direct injection into the brain (Ponzoni *et al.* 2002). Therefore, the amount of Mn^{2+} necessary in an acute dose to induce neurotoxic effects may need to exceed a specific threshold (Ponzoni *et al.* 2002). In support of this notion, Lee *et al.* (2005) demonstrated a dose-dependent response after acute Mn^{2+} administration, with doses above 88 mg kg^{-1} resulting in systemic toxicity due to the inability of the animal to regulate body temperature. Therefore, given that the doses used in our study were significantly less (40 mg kg^{-1}), it is highly unlikely that our mice were at risk for acute Mn^{2+} toxicity. In addition, multiple injections over 8 or 12 days using comparable doses had minimal to no effect on animal health, locomotion or endocrine response (Grunecker *et al.* 2010), indicating that repeat MEMRI scans may be possible without development of Mn^{2+} toxicity.

A variety of imaging modalities have been used to evaluate muscular dystrophy in humans and in animal models. Although many imaging techniques have proved clinically relevant, they rely upon the appearance of morphological alterations in muscle, such as increased

fatty infiltrates or fibrosis (Rutkove *et al.* 2014; Willcocks *et al.* 2014, 2016; Shklyar *et al.* 2015; Zaidman *et al.* 2015; Hogrel *et al.* 2016), and are limited in their ability to detect differences in individuals where these alterations are minimal or have not yet begun to take place. Here, we demonstrated that MEMRI was able to detect differences in dystrophic muscle as well as differences between dystrophic muscle and a mouse model genetically modified to alleviate the dystrophic pathology. Although this demonstrates the feasibility of using MEMRI to monitor the volume of muscle with enhanced Mn^{2+} contrast, we do not know the concentration of Mn^{2+} within the muscle. We are currently using T1 mapping and T1 relaxivity to determine the concentration of Mn^{2+} within the muscle. We showed that Mn^{2+} clearance from muscle occurred relatively quickly, which could allow for repeated imaging without an impact on muscle function or accumulation of Mn^{2+} and toxicity. Mn^{2+} appears to clear from most tissues quickly; however, future work is needed to establish the lowest dose necessary to detect differences with MEMRI and evaluate neurological function. Given that MEMRI uses the movement of Mn^{2+} (surrogate for Ca^{2+}) into a cell, an early event in the dystrophic process, it may allow for imaging of molecular alterations in dystrophic muscle across all age groups. We are currently investigating whether MEMRI can be used to differentiate disease status in young animals. Transverse relaxation time (T2)-weighted MRI imaging is a standard in the field and has been used to assess replacement of muscle with adipose tissue and oedema (Mathur *et al.* 2011; Heier *et al.* 2014). Future studies combing T2 imaging and MEMRI would provide unprecedented details of the pathological progression of the dystrophic process.

Our data indicate that eliminating Nox2 ROS in adult mice continued to protect against *in vitro* and *in vivo* aberrant calcium influx and functional deficits observed in dystrophic muscle. In combination with our previous data (Pal *et al.* 2014), enhanced Nox2-dependent ROS production in dystrophic muscle appears to play a major role in contributing to the observed alterations in calcium influx and subsequent muscle dysfunction. MEMRI is a viable, non-invasive technique to monitor dystrophic muscle and is sensitive enough to differentiate between healthy muscle, dystrophic muscle and dystrophic muscle modified to alleviate the pathology. A single administration of $MnCl_2$ was quickly cleared, did not appear to induce any toxic effects on the animal's health and had no negative effects on muscle function. Therefore, MEMRI might allow for patients to be imaged frequently, without negative consequences, and throughout their lives to evaluate and monitor disease progression. In addition, the ability of MEMRI to delineate differences in disease severity would provide a tool with which to evaluate and monitor the effectiveness of potential therapies for DMD.

References

Ahmad N, Welch I, Grange R, Hadway J, Dhanvantari S, Hill D, Lee TY & Hoffman LM (2011). Use of imaging biomarkers to assess perfusion and glucose metabolism in the skeletal muscle of dystrophic mice. *BMC Musculoskelet Disord* **12**, 127.

Altamirano F, Valladares D, Henríquez-Olguín C, Casas M, López JR, Allen PD & Jaimovich E (2013). Nifedipine treatment reduces resting calcium concentration, oxidative and apoptotic gene expression, and improves muscle function in dystrophic *mdx* mice. *PLoS ONE* **8**, e81222.

Andrews M, Giger ML & Roman BB (2015). Manganese-enhanced MRI detection of impaired calcium regulation in a mouse model of cardiac hypertrophy. *NMR Biomed* **28**, 255–263.

Barandier CE, Boucher FR & de Leiris JP (1998). Manganese reduces myocardial reperfusion injury on isolated rat heart. *J Mol Cell Cardiol* **30**, 837–847.

Beenakker EA, Maurits NM, Fock JM, Brouwer OF & van der Hoeven JH (2005). Functional ability and muscle force in healthy children and ambulant Duchenne muscular dystrophy patients. *Eur J Paediatr Neurol* **9**, 387–393.

Bushby K & Connor E (2011). Clinical outcome measures for trials in Duchenne muscular dystrophy: report from International Working Group meetings. *Clin Investig (Lond)* **1**, 1217–1235.

Cha M, Lee K, Lee C, Cho JH, Cheong C, Sohn JH & Lee BH (2016). Manganese-enhanced MR imaging of brain activation evoked by noxious peripheral electrical stimulation. *Neurosci Lett* **613**, 13–18.

Chen Y, Payne K, Perara VS, Huang S, Baba A, Matsuda T & Yu X (2012). Inhibition of the sodium–calcium exchanger via SEA0400 altered manganese-induced T_1 changes in isolated perfused rat hearts. *NMR Biomed* **25**, 1280–1285.

Close RI (1972). Dynamic properties of mammalian skeletal muscles. *Physiol Rev* **52**, 129–197.

Coassin M, Ursini F & Bindoli A (1992). Antioxidant effect of manganese. *Arch Biochem Biophys* **299**, 330–333.

De Backer F, Vandebrouck C, Gailly P & Gillis JM (2002). Long-term study of Ca^{2+} homeostasis and of survival in collagenase-isolated muscle fibres from normal and *mdx* mice. *J Physiol* **542**, 855–865.

Dietrich O, Raya JG, Reeder SB, Reiser MF & Schoenberg SO (2007). Measurement of signal-to-noise ratios in MR images: influence of multichannel coils, parallel imaging, and reconstruction filters. *J Magn Reson Imaging* **26**, 375–385.

Doctrow SR, Huffman K, Marcus CB, Tocco G, Malfroy E, Adinolfi CA, Kruk H, Baker K, Lazarowych N, Mascarenhas J & Malfroy B (2002). Salen–manganese complexes as catalytic scavengers of hydrogen peroxide and cytoprotective agents: structure–activity relationship studies. *J Med Chem* **45**, 4549–4558.

Dodd CA, Ward DL & Klein BG (2005). Basal ganglia accumulation and motor assessment following manganese chloride exposure in the C57BL/6 mouse. *Int J Toxicol* **24**, 389–397.

Dryselius S, Grapengiesser E, Hellman B & Gylfe E (1999). Voltage-dependent entry and generation of slow Ca^{2+} oscillations in glucose-stimulated pancreatic β-cells. *Am J Physiol Endocrinol Metab* **276**, E512–E518.

Durmus T, Schilling R, Doeblin P, Huppertz A, Hamm B, Taupitz M & Wagner M (2012). Gadobutrol for magnetic resonance imaging of chronic myocardial infarction: intraindividual comparison with gadopentetate dimeglumine. *Invest Radiol* **47**, 183–188.

Eybl V & Kotyzová D (2010). Protective effect of manganese in cadmium-induced hepatic oxidative damage, changes in cadmium distribution and trace elements level in mice. *Interdiscip Toxicol* **3**, 68–72.

Fan Z, Wang J, Ahn M, Shiloh-Malawsky Y, Chahin N, Elmore S, Bagnell CR Jr, Wilber K, An H, Lin W, Zhu H, Styner M & Kornegay JN (2014). Characteristics of magnetic resonance imaging biomarkers in a natural history study of golden retriever muscular dystrophy. *Neuromuscul Disord* **24**, 178–191.

Foltz CJ & Ullman-Cullere MH (1999). Guidelines for assessing the health and condition of mice. *Lab Animal* **28**, 28–32.

Franco-Obregon A Jr & Lansman JB (1994). Mechanosensitive ion channels in skeletal muscle from normal and dystrophic mice. *J Physiol* **481**, 299–309.

Gallez B, Baudelet C, Adline J, Geurts M & Delzenne N (1997). Accumulation of manganese in the brain of mice after intravenous injection of manganese-based contrast agents. *Chem Res Toxicol* **10**, 360–363.

Gerdin BB (1985). Selective tissue accumulation of manganese and its effect on regional blood flow and haemodynamics after intravenous infusion of its chloride salt in the rat. *Int J Tissue React* **7**, 373–380.

Grunecker B, Kaltwasser SF, Peterse Y, Samann PG, Schmidt MV, Wotjak CT & Czisch M (2010). Fractionated manganese injections: effects on MRI contrast enhancement and physiological measures in C57BL/6 mice. *NMR Biomed* **23**, 913–921.

Heier CR, Guerron AD, Korotcov A, Lin S, Gordish-Dressman H, Fricke S, Sze RW, Hoffman EP, Wang P & Nagaraju K (2014). Non-invasive MRI and spectroscopy of *mdx* mice reveal temporal changes in dystrophic muscle imaging and in energy deficits. *PLoS One* **9**, e112477.

Hogrel JY, Wary C, Moraux A, Azzabou N, Decostre V, Ollivier G, Canal A, Lilien C, Ledoux I, Annoussamy M, Reguiba N, Gidaro T, Le Moing AG, Cardas R, Voit T, Carlier PG & Servais L (2016). Longitudinal functional and NMR assessment of upper limbs in Duchenne muscular dystrophy. *Neurology* **86**, 1022–1030.

Hu TCC, Chuang K-H, Yanasak N & Koretsky A (2011). Relation between blood and cardiac manganese during manganese-enhanced magnetic resonance imaging (MEMRI) with T_1 mapping in the rodent. *NMR Biomed* **24**, 46–53.

Inoue T, Majid T & Pautler RG (2011). Manganese enhanced MRI (MEMRI): neurophysiological applications. *Rev Neurosci* **22**, 675–694.

Kato M (1963). Distribution and excretion of radiomanganese administered to the mouse. *Q J Exp Physiol Cogn Med Sci* **48**, 355–369.

Kim JH & Lawler JM (2012). Amplification of proinflammatory phenotype, damage, and weakness by oxidative stress in the diaphragm muscle of *mdx* mice. *Free Radic Biol Med* **52**, 1597–1606.

Kozakowska M, Pietraszek-Gremplewicz K, Jozkowicz A & Dulak J (2015). The role of oxidative stress in skeletal muscle injury and regeneration: focus on antioxidant enzymes. *J Muscle Res Cell Motil* **36**, 377–393.

Lee JH, Silva AC, Merkle H & Koretsky AP (2005). Manganese-enhanced magnetic resonance imaging of mouse brain after systemic administration of $MnCl_2$: dose-dependent and temporal evolution of T_1 contrast. *Magn Reson Med* **53**, 640–648.

Levi O, Genin O, Angelini C, Halevy O & Pines M (2015). Inhibition of muscle fibrosis results in increases in both utrophin levels and the number of revertant myofibers in Duchenne muscular dystrophy. *Oncotarget* **6**, 23249–23260.

Majid T, Ali YO, Venkitaramani DV, Jang MK, Lu HC & Pautler RG (2014). *In vivo* axonal transport deficits in a mouse model of fronto-temporal dementia. *Neuroimage Clin* **4**, 711–717.

Mathur S, Vohra RS, Germain SA, Forbes S, Bryant ND, Vandenborne K & Walter GA (2011). Changes in muscle T_2 and tissue damage after downhill running in mdx mice. *Muscle Nerve* **43**, 878–886.

Naruse K & Sokabe M (1993). Involvement of stretch-activated ion channels in Ca^{2+} mobilization to mechanical stretch in endothelial cells. *Am J Physiol Cell Physiol* **264**, C1037–C1044.

Ni Y, Petre C, Bosmans H, Miao Y, Grant D, Baert AL & Marchal G (1997). Comparison of manganese biodistribution and MR contrast enhancement in rats after intravenous injection of MnDPDP and $MnCl_2$. *Acta Radiol* **38**, 700–707.

Ortolan P, Zanato R, Coran A, Beltrame V & Stramare R (2015). Role of radiologic imaging in genetic and acquired neuromuscular disorders. *Eur J Transl Myol* **25**, 5014.

Pal R, Palmieri M, Loehr JA, Li S, Abo-Zahrah R, Monroe TO, Thakur PB, Sardiello M & Rodney GG (2014). Src-dependent impairment of autophagy by oxidative stress in a mouse model of Duchenne muscular dystrophy. *Nat Commun* **5**, 4425.

Ponzoni S, Gaziri LCJ, Britto LRG, Barreto WJ & Blum D (2002). Clearance of manganese from the rat substantia nigra following intra-nigral microinjections. *Neurosci Lett* **328**, 170–174.

Ray MA, Johnston NA, Verhulst S, Trammell RA & Toth LA (2010). Identification of markers for imminent death in mice used in longevity and aging research. *J Am Assoc Lab Anim Sci* **49**, 282–288.

Rodriguez O, Schaefer ML, Wester B, Lee YC, Boggs N, Conner HA, Merkle AC, Fricke ST, Albanese C & Koliatsos VE (2016). Manganese-enhanced magnetic resonance imaging as a diagnostic and dispositional tool after mild-moderate blast traumatic brain injury. *J Neurotrauma* **33**, 662–671.

Rutkove SB, Geisbush TR, Mijailovic A, Shklyar I, Pasternak A, Visyak N, Wu JS, Zaidman C & Darras BT (2014). Cross-sectional evaluation of electrical impedance myography and quantitative ultrasound for the assessment of Duchenne muscular dystrophy in a clinical trial setting. *Pediatr Neurol* **51**, 88–92.

Schroeder MP, Weiss C, Procissi D, Wang L & Disterhoft JF (2016). Activity-induced manganese-dependent MRI (AIM-MRI) and functional MRI in awake rabbits during somatosensory stimulation. *NeuroImage* **126**, 72–80.

Shklyar I, Geisbush TR, Mijialovic AS, Pasternak A, Darras BT, Wu JS, Rutkove SB & Zaidman CM (2015). Quantitative muscle ultrasound in Duchenne muscular dystrophy: a comparison of techniques. *Muscle Nerve* **51**, 207–213.

Sotogaku N, Oku N & Takeda A (2000). Manganese concentration in mouse brain after intravenous injection. *J Neurosci Res* **61**, 350–356.

Takeda A (2003). Manganese action in brain function. *Brain Res Brain Res Rev* **41**, 79–87.

Takeda A, Sawashita J & Okada S (1998). Manganese concentration in rat brain: manganese transport from the peripheral tissues. *Neurosci Lett* **242**, 45–48.

Tutdibi O, Brinkmeier H, Rüdel R & Föhr KJ (1999). Increased calcium entry into dystrophin-deficient muscle fibres of MDX and ADR-MDX mice is reduced by ion channel blockers. *J Physiol* **515**, 859–868.

Vasquez I, Tan N, Boonyasampant M, Koppitch KA & Lansman JB (2012). Partial opening and subconductance gating of mechanosensitive ion channels in dystrophic skeletal muscle. *J Physiol* **590**, 6167–6185.

Vohra RS, Mathur S, Bryant ND, Forbes SC, Vandenborne K & Walter GA (2016). Age-related T2 changes in hindlimb muscles of mdx mice. *Muscle Nerve* **53**, 84–90.

Waghorn B, Yang Y, Baba A, Matsuda T, Schumacher A, Yanasak N & Hu TC (2009). Assessing manganese efflux using SEA0400 and cardiac T1-mapping manganese-enhanced MRI in a murine model. *NMR Biomed* **22**, 874–881.

Whitehead NP, Pham C, Gervasio OL & Allen DG (2008). *N*-Acetylcysteine ameliorates skeletal muscle pathophysiology in *mdx* mice. *J Physiol* **586**, 2003–2014.

Whitehead NP, Yeung EW, Froehner SC & Allen DG (2010). Skeletal muscle NADPH oxidase is increased and triggers stretch-induced damage in the *mdx* mouse. *PloS One* **5**, e15354.

Willcocks RJ, Arpan IA, Forbes SC, Lott DJ, Senesac CS, Senesac E, Deol J, Triplett W, Baligand C, Daniels MJ, Sweeney HL, Walter GA & Vandenborne K (2014). Longitudinal measurements of MRI-T_2 in boys with Duchenne muscular dystrophy: effects of age and disease progression. *Neuromusc Disord* **24**, 393–401.

Willcocks RJ, Rooney WD, Triplett WT, Forbes SC, Lott DJ, Senesac CR, Daniels MJ, Wang DJ, Harrington AT, Tennekoon GI, Russman BS, Finanger EL, Byrne BJ, Finkel RS, Walter GA, Sweeney HL & Vandenborne K (2016). Multicenter prospective longitudinal study of magnetic resonance biomarkers in a large Duchenne muscular dystrophy cohort. *Ann Neurol* **79**, 535–547.

Yamada T, Abe M, Lee J, Tatebayashi D, Himori K, Kanzaki K, Wada M, Bruton JD, Westerblad H & Lanner JT (2015). Muscle dysfunction associated with adjuvant-induced arthritis is prevented by antioxidant treatment. *Skelet Muscle* **5**, 20.

Yang J, Li Q, Wang M, Cao X, Ding Y, Wang G & Liao C (2016). Semiquantitative assessment of optic nerve injury using manganese-enhanced MRI. *Jpn J Radiol* **34**, 356–365.

Zaidman CM, Malkus EC & Connolly AM (2015). Muscle ultrasound quantifies disease progression over time in infants and young boys with Duchenne muscular dystrophy. *Muscle Nerve* **52**, 334–338.

Zhao DW, Zhang LT, Cheng HY, Zhang YL, Min JY, Xiao HL & Wang Y (2015). Monitoring dynamic alterations in calcium homeostasis by T1-mapping manganese-enhanced MRI (MEMRI) in the early stage of small intestinal ischemia-reperfusion injury. *NMR Biomed* **28**, 958–966.

Additional information

Competing interests

None declared.

Author contributions

G.G.R., J.A.L., R.G.P., G.R.S. and L.J.W. were involved with the conception and design of the experiments. J.A.L., G.R.S., W.T.R. and M.H.-R. acquired the data. All authors were involved in the analysis and interpretation of the data and provided critical input to the writing and revisions of the manuscript. All authors approved the final version of the manuscript and agree to be accountable for all aspects of the work in ensuring that questions related to the accuracy or integrity of any part of the work are appropriately investigated and resolved. All persons designated as authors qualify for authorship, and all those who qualify for authorship are listed.

Funding

Research reported in this publication was supported by the National Institute of Arthritis and Musculoskeletal and Skin Diseases of the National Institutes of Health (R01 AR061370, to G.G.R.), the National Institute of Neurological Disorders and Stroke of the National Institutes of Health (R21 NS085208, to R.G.P. and G.G.R.), the National Heart, Lung, and Blood Institute of the National Institutes of Health (T32 HL007676, to J.A.L.) and a Gillson Longenbaugh Foundation Award (G.G.R.). Additional support was provided by the Welch Foundation (C-0627, to L.J.W.).

Acknowledgements

The authors would like to thank Drs Glen Walter and Joe Kornegay for their critical discussions and suggestions.